AGU ADVANCING EARTH AND SPACE SCIENCES

Geophysical Research Letters

RESEARCH LETTER
10.1029/2025GL118423

State-Dependence of Polar Amplification in an Idealized GCM

Andrew I. L. Williams[1,2] and **Timothy M. Merlis**[1]

[1]Program in Atmospheric and Oceanic Sciences, Princeton University, Princeton, NJ, USA, [2]Scripps Institution of Oceanography, University of California San Diego, La Jolla, CA, USA

Key Points:

- Polar amplification (PA) is simulated in a wide range of climate states using an idealized moist atmospheric general circulation model
- In the absence of ice-albedo feedbacks, PA increases with increasing global-mean temperature and equator-to-pole temperature contrast
- On top of this, including an ice-albedo feedback amplifies PA in climates where the climatological ice-edge lies within the polar cap

Supporting Information:

Supporting Information may be found in the online version of this article.

Correspondence to:

A. I. L. Williams,
andrewwilliams@ucsd.edu

Citation:

Williams, A. I. L., & Merlis, T. M. (2026). State-dependence of polar amplification in an idealized GCM. *Geophysical Research Letters*, *53*, e2025GL118423. https://doi.org/10.1029/2025GL118423

Received 23 JUL 2025
Accepted 22 DEC 2025

Abstract Polar amplification (PA) is a robust feature of contemporary climate change, but its state-dependence across different climate conditions is poorly understood despite potential relevance to paleoclimate records and future projections. Here we examine the state-dependence of PA across a wide range of climate states in an idealized moist general circulation model. We generate a phase space of climate states with different global-mean surface temperatures and equator-to-pole surface temperature contrasts then perturb each with longwave radiative forcing. We find that the state-dependence of PA is largely a superposition of two effects. Firstly, as a consequence of moist thermodynamics, latent energy transport drives stronger PA in climates with higher global-mean surface temperatures and stronger meridional surface temperature gradients. On top of this, the ice-albedo feedback amplifies PA in climates where the climatological ice edge sits within the polar cap.

Plain Language Summary In response to global warming, the polar regions typically warm more than the tropics; this is called "polar amplification." Using simplified climate model experiments, we systematically tested how this polar amplification depends on two fundamental climate properties: the planet's overall temperature and the temperature difference between equator and poles. We find that polar amplification becomes stronger in warmer worlds and when temperature contrasts are larger, primarily because the atmosphere becomes more efficient at transporting energy to the polar regions as warm air holds more moisture. In addition to this, we find that the melting of ice (which exposes darker oceans underneath) can strengthen polar amplification if the ice-edge sits within the polar regions.

1. Introduction

The pattern of surface temperature change in response to radiative forcing often has a polar-amplified pattern, with more warming at high latitudes than low latitudes. Multiple mechanisms can give rise to polar amplification (PA) under warming, including the effects of sea ice loss, increased atmospheric energy transport, and a locally destabilizing atmospheric lapse rate feedback (as reviewed by Taylor et al., 2022). Extensive analysis of PA exists in comprehensive climate model projections of future climate (e.g., Hahn et al., 2021; Hwang et al., 2011; Winton, 2006), and it appears in both cold paleoclimate states, like the Last Glacial Maximum (Masson-Delmotte et al., 2006), and hot paleoclimate states, like the Eocene (Henry & Vallis, 2022; Huber & Caballero, 2011). The ubiquity of PA across vastly different climate states raises fundamental questions about whether the magnitude and mechanisms of PA depend on the base climate state itself. Understanding such state-dependence is useful for interpreting paleoclimate records and assessing how PA might evolve as the climate warms.

A common theoretical tool for studying the pattern of surface temperature change is one-dimensional, diffusive moist energy balance models (MEBMs) (e.g., Bonan et al., 2018; Flannery, 1984; Roe et al., 2015; Rose et al., 2014). Previous work has shown that MEBMs predict state-dependent PA, with larger PA when the base state has warmer global-mean surface temperature and/or stronger meridional temperature gradients (Merlis & Henry, 2018). The MEBM's state-dependence arises because of the well-established state-dependence of latent energy transport changes (e.g., Caballero & Langen, 2005; Guendelman & Kaspi, 2020; Hahn et al., 2023; Kaspi & Showman, 2015; Merlis et al., 2022; O'Gorman & Schneider, 2008a). Latent energy transport depends on meridional moisture gradients and thus derives a state-dependence from the exponential nature of the Clausius-Clapeyron relationship. In climates that are initially warm and/or have strong meridional temperature gradients, warming produces a greater increase in meridional moisture gradients and consequently, greater latent energy transport changes.

While MEBMs predict state-dependent PA, their simplified representations of atmospheric energy transport means it is not clear if this prediction holds in more comprehensive models where atmospheric energy transport is explicitly resolved. Furthermore, it is not clear how spatially-varying, state-dependent temperature and albedo feedbacks (factors typically neglected in MEBMs) modify the state-dependence of PA. To tackle these questions, here we move to the next "rung" in climate model hierarchy (Held et al., 2005; Jeevanjee et al., 2017; Maher et al., 2019) and examine the state-dependence of PA in a series of idealized moist GCM simulations which have resolved atmospheric energy transport, gray radiative transfer, and a simple representation of the ice-albedo feedback. The simulations span a range of global-mean temperatures and equator-to-pole temperature contrasts and include both past Earth analogs and more exotic climate states. Our focus on state-dependence of PA extends previous work which has used idealized GCM simulations to shed light on the role of atmospheric processes in driving contemporary PA (e.g., Feldl & Merlis, 2021; Henry & Merlis, 2019; Langen et al., 2012; Lu et al., 2022; Merlis et al., 2022).

We proceed as follows: In the next section, we present the idealized GCM model configuration and the results of the series of simulations where the base-state global-mean surface temperature and equator-to-pole meridional surface temperature contrast are varied. We then present an analysis of the local atmospheric energy budget, expressed as a surface warming. The conclusion discusses different ways of combining the local energy budget components and the role of omitted processes in the idealized GCM.

2. Idealized GCM

2.1. Overview

The idealized aquaplanet GCM used in this work is a configuration of Isca (Vallis et al., 2018) that follows closely Frierson et al. (2006) and O'Gorman and Schneider (2008b). The representation of physical processes in the atmosphere is idealized in several ways. The radiation is represented by a gray scheme (no cloud or water vapor radiative effects) and the "microphysics" is a saturation adjustment to 100% relative humidity using an idealized formulation of the Clausius–Clapeyron relation with the condensed water assumed to instantaneously fall to the surface as precipitation (i.e., there are no condensed water phases in the atmosphere). We also only consider vapor–liquid phase change (i.e., there is no ice in the atmosphere). A simplified Betts-Miller scheme relaxes convectively unstable profiles toward a moist adiabat with a 2-hr timescale (Frierson, 2007). The insolation, I, is a time-independent function of latitude, ϕ, that approximates a perpetual annual-mean,

$$I(\phi) = \frac{S_0}{4}\left[1 + \frac{\Delta_s}{4}\left(1 - 3\sin^2(\phi)\right)\right], \tag{1}$$

where $S_0 = 1360\ \mathrm{Wm}^{-2}$, and $\Delta_s = 1.4$ (Frierson et al., 2006). There is no atmospheric absorption of solar radiation. To perturb the climate, the longwave optical depth is increased by 40%, following Henry and Merlis (2019), yielding a global-mean radiative forcing of $\approx 20\ \mathrm{Wm}^{-2}$.

The lower boundary condition is a slab ocean with a heat capacity of 20 m of water that allows for rapid equilibration. We conducted two sets of simulations, one with a fixed surface albedo of 0.22 which suppresses any ice-albedo feedbacks, and one with a temperature-dependent surface albedo which mimics the ice-albedo feedback. The temperature-dependent surface albedo, α_s, follows Eisenman and Wettlaufer (2009):

$$\alpha_s(T) = \frac{\alpha_0 + \alpha_i}{2} + \frac{\alpha_0 - \alpha_i}{2}\tanh\left(\frac{T - T_{\mathrm{edge}}}{h}\right) \tag{2}$$

so that α_s gradually varies from an open water value, α_0, to a sea ice value, α_i, with smoothness parameter h. We set $\alpha_0 = 0.22$, $\alpha_i = 0.5$, $h = 6$ K, and $T_{\mathrm{edge}} = -11$°C is the temperature at the center of the albedo transition zone. Note the ice albedo value is low to keep the TOA albedo change similar to Earth's because of the lack of atmospheric reflection (e.g., clouds are not attenuating the downward shortwave).

Our model does not represent the thermodynamic effects of sea ice, which have previously been shown to suppress summer warming and enhance winter warming by enabling a seasonal redistribution of energy through the growth and melting of sea ice (Deser et al., 2010; Feldl & Merlis, 2021; Hahn et al., 2022; Manabe &

Stouffer, 1980). However, these thermodynamic effects are primarily seasonal and previous work has shown that, in the annual-mean, the impact of sea ice thinning on polar amplification is small (P.-C. Chung & Feldl, 2024; England et al., 2022; Feldl & Merlis, 2021). Hence, given that we are examining climates without seasonal cycles, it is reasonable to represent only the albedo effects of sea ice. Future studies could build on our work by including sea ice thermodynamics in an idealized GCM and examining the state-dependence of seasonally-varying PA.

All simulations are performed at T42 spectral truncation ($\approx 2.8°$ horizontal resolution) with 50 vertical levels in the model's sigma (pressure divided by surface pressure) coordinate and are integrated for 3,000 days. The analysis is conducted over the final 1,500 days once the simulations have reached steady-state. A prescribed ocean energy source/sink term allows us to generate a wide range of climate base states, which is described next.

We use a gray radiation scheme—as opposed to Isca's correlated-k radiation scheme, RRTMG (Mlawer et al., 1997)—to prevent errors associated with out-of-bounds usage of RRTMG (Kluft et al., 2019) when we explore more extreme climate states. Another approach would be to use a radiation scheme which is validated at these extreme temperatures, for example, the SOCRATES scheme (Manners et al., 2017). However, using a gray radiation scheme greatly simplifies the calculation of radiative feedbacks compared to a more comprehensive scheme like SOCRATES, in addition to minimizing the computational expense.

2.2. Generating a Wide Range of Base States

The use of slab ocean boundary conditions is critical to allow the perturbed climates to develop an energetically consistent pattern of surface temperature change. Therefore, we need a systematic method for generating control climates with different global-mean and temperature gradients. To do so, we first perform simulations with prescribed sea surface temperature (SST) and use the equilibrated surface energy budget to determine the Q-flux that would generate that climate in a slab ocean simulation. The fixed-SST simulations are run for 1500 days, with analysis conducted over the final 200 days. Typically, a Q-flux represents the divergence of the vertically integrated ocean energy transport, which would have zero global mean. Here, because we are using the imposed Q-flux to alter both the global-mean SST and its meridional structure, the Q-flux can have a non-zero global-mean value.

Simulations with prescribed sea surface temperature (SST) are performed using the following idealized function:

$$\mathrm{SST}(\phi) = T_0 + \frac{\Delta_h}{3}\left[3\sin^2(\phi) - 1\right], \tag{3}$$

with global-mean SST, T_0, and the equator-to-pole contrast, Δ_h. The imbalance between the net turbulent surface fluxes F_s and the net surface radiation R_s determines the Q-flux Q. In other words, the equilibrium surface energy budget of these prescribed SST simulations is $Q = F_s + R_s$. This Q can then be prescribed in a slab ocean boundary condition to reproduce the SST given by Equation 3. The slab ocean model is then perturbed with the increased longwave optical depth to examine how the pattern of the forced response of surface temperature varies with the control surface temperature distribution. The global-mean surface temperatures span 270 to 300 K and the equator-to-pole contrasts span 15 to 90 K.

The climate states explored here include past Earth analogs such as hot, Eocene-like climates with weak equator-to-pole contrasts (e.g., Henry & Vallis, 2022) and cold climates with strong equator-to-pole contrasts such during the late Paleozoic (e.g., Judd et al., 2024) or during the Cryogenian (e.g., Pierrehumbert et al., 2011). Our simulations also include states without obvious analogs in Earth's history, such as very warm climates with strong equator-to-pole contrasts. However, such climates may exist in an exoplanet context through some combination of increased insolation/CO_2 and high planetary rotation rate (e.g., Kaspi & Showman, 2015).

For each fixed-SST simulation used to calculate the Q-flux, we also conduct another fixed-SST simulation with increased longwave optical depth. The effective radiative forcing is calculated as the difference in top-of-atmosphere radiation between the fixed-SST simulation with increased optical depth and the control fixed-SST simulation.

Because of the symmetries of the boundary conditions the simulated climates are zonally and hemispherically symmetric. We thus average all fields zonally and between the hemispheres and only present results for 0–90° latitude.

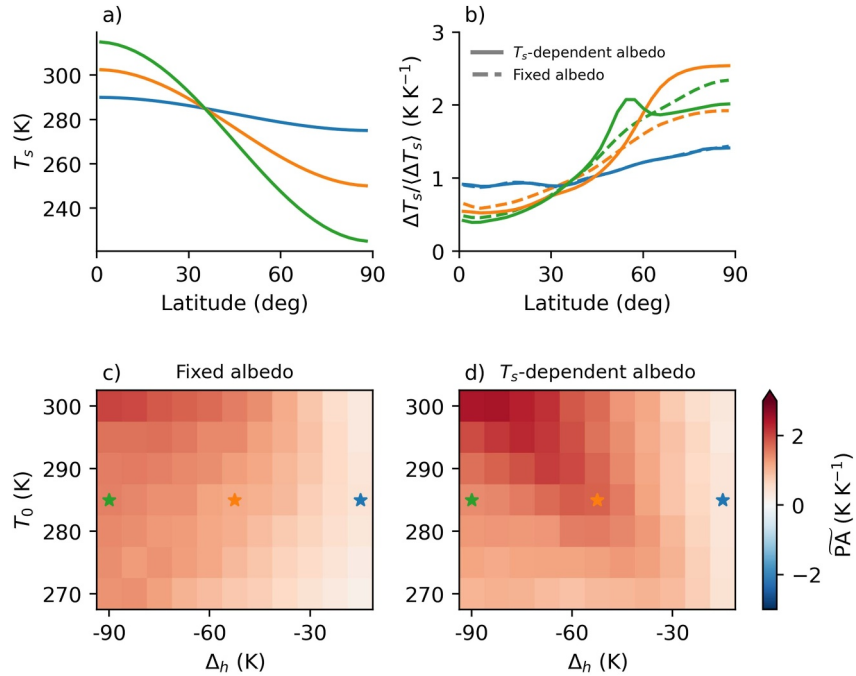

Figure 1. (a) Zonal-mean surface temperatures in the control simulation, for three values of the global-mean temperature and equator-to-pole temperature contrast indicated by the colored stars in panels (c and d). (b) Pattern of surface temperature change for these three base climate states as simulated by the idealized GCM with fixed surface albedo (dashed), and a temperature-dependent surface albedo (solid). (c and d) The state-dependence of a PA metric (Equation 4) for a wide range of base climate states, where the global-mean surface temperature (vertical axis) and equator-to-pole surface temperature contrast (horizontal axis) are varied for. Panel (c) is for the simulations with fixed albedo, and panel (d) is for the simulations with a temperature-dependent surface albedo. The temperature change patterns and metrics in panels (b–d) are normalized by the global-mean surface temperature change, and hence have units of K K^{-1}.

3. Simulated State-Dependence of PA

3.1. Idealized GCM Results

Figure 1a shows the control SST profiles for three values of the global-mean surface temperature and equator-to-pole contrast (shown as stars in Figure 1c); the orange curve represents an approximately "Earth-like" climate, while the other curves represent climates with the same global-mean surface temperature but much stronger/weaker equator-to-pole contrasts. Figure 1b shows the change in surface temperature per degree of global-mean warming in response to increased optical depth for each of these three base states. Dashed lines denote the simulations with fixed surface albedo, and solid lines denote simulations with a temperature-dependent surface albedo which mimics an ice-albedo feedback. Visually, it is clear that different base climate states can have very different amounts of polar amplification. For example, the Earth-like base climate has approximately 1.8 times as much warming in the polar regions (poleward of 60° latitude) than in the global mean under fixed albedo, increasing to 2.4 times when an ice-albedo feedback is enabled (Figure 1b, orange line). On the other hand, in a climate with the same global-mean temperature but a much weaker equator-to-pole contrast, the poles only warm about 1.3 times more than the global-mean (Figures 1a and 1b, blue line). Ice-albedo feedback affects the degree of polar amplification substantially in the "Earth-like climate," but has weaker effects in the illustrative climates with altered meridional temperature gradients.

To illustrate PA's state-dependence over the full range of simulations, we define a PA metric, $\widetilde{\mathrm{PA}}$. This metric is the difference between a polar cap and tropical average, normalized by the global-mean surface temperature:

$$\widetilde{\mathrm{PA}} \equiv \frac{\Delta T_s|_{\mathrm{pole}}}{\langle \Delta T_s \rangle} - \frac{\Delta T_s|_{\mathrm{trop}}}{\langle \Delta T_s \rangle}, \tag{4}$$

with the polar cap bounded by 60° and the tropical average taken within 30° of the equator. Angle brackets denote an area-weighted global average. The appeal of normalizing by the global-mean surface temperature change is that there is some state-dependence in this model's climate sensitivity (due to state-dependence of the Planck feedback): it varies from ≈ 4 to ≈ 6 K for this change in optical depth. Eliminating this climate sensitivity variation isolates the pattern of warming.

Figures 1c and 1d shows $\widetilde{\mathrm{PA}}$ over the range of climates with varied global-mean surface temperature (vertical axis) and varied equator-to-pole surface temperature contrast (horizontal axis). The simulations with a fixed, uniform surface albedo are shown in panel c, and the interactive albedo simulations are shown in panel d. In the absence of an ice-albedo feedback, PA is generally larger in climates with warmer global-mean surface temperatures and/or greater meridional temperature gradients, and these tendencies are largely monotonic (Figure 1c). This behavior matches the predictions from the previous MEBM theory (Figure S1 in Supporting Information S1). Simulations including an ice-albedo feedback are broadly similar, but also have enhanced PA along the locus of climates which connect the upper-left and bottom-right of the phase space. The goal of this paper is to explain this tendency toward larger PA in warmer climates with stronger equator-to-pole temperature gradients, and how this is modulated by ice-albedo feedbacks.

4. Local Energy Budget Analysis

4.1. Method

To better understand what drives the state-dependence of PA in our simulations, we follow previous studies (with the earliest examples being Crook et al., 2011; Feldl & Roe, 2013; Lu & Cai, 2009; Winton, 2006) and evaluate the local atmospheric energy budget contributions to local temperature change. In this framework, the local temperature change is a function of the radiative forcing $\mathcal{F}$, local radiative feedbacks λ_i, and divergence of the moist static energy (h) flux:

$$\Delta T_s = \frac{-\mathcal{F} + \Delta(\nabla \cdot \{\mathbf{u}h\}) - \Delta T_s \Sigma_i \lambda_i}{\langle \lambda_P \rangle}, \tag{5}$$

with Planck feedback λ_P, global mean indicated by $\langle \cdot \rangle$, and column integral indicated by $\{\cdot\}$. The sum over feedbacks includes the spatially varying component of the Planck feedback, the lapse rate feedback, and the surface albedo feedback. In comprehensive GCMs, λ_i would also include relative humidity and cloud feedbacks.

The vertically integrated divergence of meridional atmospheric energy transport is determined from the steady-state atmospheric energy budget:

$$\nabla \cdot \{\mathbf{u}h\} = N - Q, \tag{6}$$

with net radiation N and Q-flux Q (i.e., the sum of the surface energy fluxes). Analogously, the vertically integrated divergence of meridional latent energy transport is obtained from the precipitation minus evaporation (multiplied by the latent heat of vapourization); dry energy transport is a residual of the total and latent terms. The total feedback is calculated using the perturbation TOA budget:

$$\lambda(\phi) = \frac{-\mathcal{F} + \Delta(\nabla \cdot \{\mathbf{u}h\})}{\Delta T_s}. \tag{7}$$

The Planck feedback is calculated by an additional online call to the radiative transfer scheme with the temperature field perturbed by 1K uniformly throughout the atmosphere (Merlis et al., 2022). The surface albedo feedback is calculated using the surface albedo and the top-of-atmosphere insolation—equivalent to downward surface shortwave because the GCM's atmosphere is transparent to shortwave radiation. The lapse-rate feedback is calculated as a residual of the total feedback, defined by Equation 7, and the sum of the Planck and surface albedo feedbacks; the estimated lapse-rate feedback thus includes errors which may arise from non-linearities neglected by Equation 7.

10.1029/2025GL118423

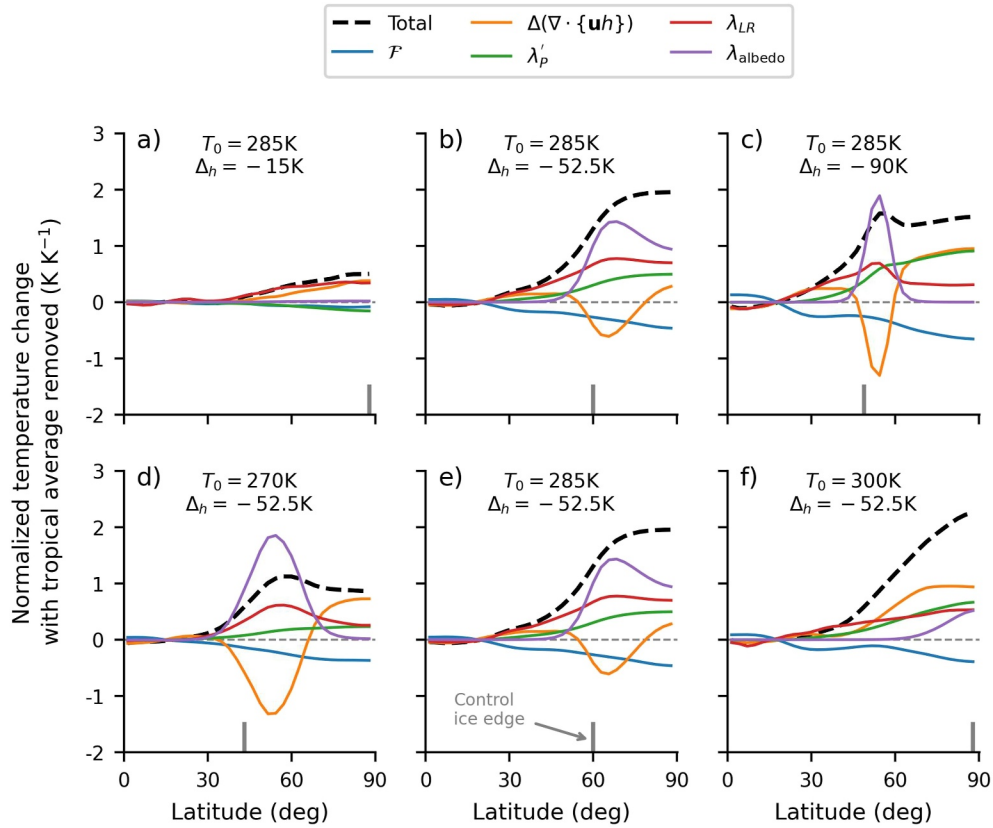

Figure 2. Local energy budget analysis of temperature changes versus latitude for five different base state climates. Note that panels (b) and (e) are identical. Panels (a–c) show the impact of changing equator-to-pole temperature contrast, and panels (d–f) show the impact of changing global-mean temperature. The colors correspond to different components as indicated in the legend and described in Section 4.1 and Equation 5. Temperature changes have been normalized by the global-mean warming, and have the tropical-average removed so as to focus on the contributions to $\widetilde{\text{PA}}$ following Equation 4. The latitude of the ice-edge in the control climate, defined as the latitude where $SST = T_{\text{edge}}$, is shown in a gray line at the bottom of each panel.

4.2. Illustrative Cases

Figure 2 shows a select number of local energy budget analyses (Equation 5) for five illustrative climate states (panels b and e are identical). All temperature changes are normalized by the global-mean temperature change and have had the tropical-average removed so as to highlight their contribution to $\widetilde{\text{PA}}$, as defined in Equation 4. The top row of Figure 2 shows the energy budget decomposition for three values of the equator-to-pole temperature contrast, at the global-mean surface temperature of 285 K. The bottom row shows the same, but for three values of the global-mean temperature, at a constant equator-to-pole temperature contrast of 52.5 K.

To orient ourselves, we focus on the approximately "Earth-like" base state ($T_0 = 285\,\text{K}$, $\Delta_h = -52.5\,\text{K}$), which has a polar amplification index of $\widetilde{\text{PA}} \approx 2\ \text{KK}^{-1}$. The radiative forcing is tropically amplified (blue line) somewhat offsetting polar amplification, while the spatially-varying Planck feedback (green) and the lapse-rate feedback (red) have a polar amplified structure. The local temperature contributions with the most striking meridional structure are from the surface albedo feedback (purple) and the changes in the divergence of atmospheric energy transport (orange). The surface albedo feedback contributes a large positive temperature change which peaks near the latitude where $\text{SST} = T_{\text{edge}} = -11°\text{C}$ in the control climate (which is where albedo is most sensitive to temperature, by Equation 2). This "bump" from the surface albedo feedback is largely, but not perfectly, offset by an anomalous divergence of atmospheric energy transport ($\Delta(\nabla \cdot \{\mathbf{u}h\}) > 0$). This anomalous divergence atmospheric energy transport yields a local cooling response because the temperature contribution from changes in atmospheric energy transport $= \Delta(\nabla \cdot \{\mathbf{u}h\})/\langle \lambda_P \rangle$, and $\langle \lambda_P \rangle < 0$. The lapse-rate feedback is locally amplified in the vicinity of the surface albedo feedback.

Looking across climate states we see that the radiative forcing increases between panels (a) and (b) of Figure 2, but otherwise is not strongly state-dependent. The local temperature change from the spatially-varying Planck feedback increases strongly with increasing equator-to-pole temperature contrast (Figures 2a–2c), and more weakly with increasing global-mean surface temperature change (Figures 2d–2f). This can be understood by noting that, for a gray radiation scheme such as ours, the outgoing longwave radiation perturbation from a unit of warming is $\approx \left(4\sigma \overline{T}_{em}^{3}\right) \times 1\,\mathrm{K}$, with emission temperature T_{em} defined as the level where the longwave optical depth is unity. The gray radiation scheme uses optical depths which are fixed functions of pressure and thus T_{em} occurs at a fixed pressure for each latitude (for more details see Frierson et al., 2006). The meridional structure of T_{em} is generally tied to the meridional structure of surface temperature, such that the contribution of the spatially-varying Planck feedback to $\widetilde{\mathrm{PA}}$ scales with the global-mean temperature and equator-to-pole contrast. The exception to this is for climates with very weak equator-to-pole contrasts, where the spatially-varying Planck feedback weakly offsets $\widetilde{\mathrm{PA}}$ because the climatological T_{em} is warmer at the poles than the equator (not shown).

The contribution of surface albedo changes to temperature is state-dependent in two key ways. First, the location of the temperature "bump" induced by surface albedo changes shifts in line with the control climate's ice edge (e.g., as the ice edge shifts from the pole to the midlatitudes in Figures 2a–2c). Second, the magnitude of the albedo-induced warming increases as the ice edge moves more equatorward (e.g., compare purple lines in Figures 2d and 2e); similar behavior was also seen in an early study by Holland and Bitz (2003).

We can gain some analytic insights into the temperature contribution from surface albedo changes by leveraging our simple formulation of the ice-albedo feedback (Equation 2). Specifically we can derive an estimate for the size of the surface albedo temperature "bump" at the climatological ice edge (for a derivation, see Text S2 in Supporting Information S1),

$$\left.\frac{dT_{\mathrm{albedo}}}{d\langle T_s\rangle}\right|_{\mathrm{edge}} \approx \left(\frac{\alpha_0-\alpha_i}{2h}\right)\frac{I(T_{\mathrm{edge}})}{\langle\lambda_P\rangle}, \tag{8}$$

where $\alpha_0 = 0.22$, $\alpha_i = 0.5$, and $h = 6$ K, and we have normalized the temperature contribution from surface albedo changes by the global-mean warming, in keeping with Figure 2. Note that the tropical temperature contribution from the surface albedo feedback is near zero, so the purple curves in Figure 2 are equivalent to $dT_{\mathrm{albedo}}/d\langle T_s\rangle$.

Equation 8 predicts that the ice-albedo feedback causes a local warming because $\alpha_i > \alpha_0$ and $\langle\lambda_P\rangle < 0$. Next, we can use Equation 8 to get an order-of-magnitude estimate of the local albedo-induced temperature change per degree of global warming. To do this we note that, for the "Earth-like" climate with $T_0 = 285\,\mathrm{K}$ and $\Delta_h = -52.5\,\mathrm{K}$, $I(T_{\mathrm{edge}}) \approx 185\ \mathrm{Wm}^{-2}$ and $\langle\lambda_P\rangle \approx -4\ \mathrm{Wm}^{-2}\ \mathrm{K}^{-1}$. Plugging these values into Equation 8 yields $\approx 1\ \mathrm{KK}^{-1}$, in rough agreement with our simulated results in Figure 2. Equation 8 tells us that this value should scale with $\alpha_0 - \alpha_i$, and $1/h$. Thus, if we had chosen surface albedo to vary more slowly with temperature (larger h), then the ice-albedo feedback would contribute a smaller temperature change, and if we had chosen parameters such that $\alpha_0 - \alpha_i$ was larger the ice-albedo feedback would contribute a larger temperature change.

Equation 8 can also explain why the albedo contribution increases in colder climates (smaller T_0) and with increased magnitude of Δ_h (Figure 2). This is because $I(T_{\mathrm{edge}})$ has same dependence on T_0 and Δ_h; colder climates with stronger equator-to-pole temperature contrasts have their ice edge closer to the equator and thus and a larger top-of-atmosphere insolation at that latitude.

The localized temperature "bump" from the surface albedo feedback is largely, but not perfectly, offset by changes in the divergence of atmospheric energy transport. This cancellation occurs through the dry component of the energy transport, not the latent component (Figure S2 in Supporting Information S1). This cancellation between changes in dry transport and the surface albedo feedback has been seen in previous work (e.g., Feldl & Roe, 2013; Hwang et al., 2011), and can be understood by modeling the divergence of atmospheric dry static energy transport, $\nabla\cdot\{\mathbf{u}s\}$, as down-gradient diffusion of near-surface temperature,

$$\nabla\cdot\{\mathbf{u}s\} = -c_p\frac{d}{dx}\left[\mathcal{D}\left(1-x^2\right)\frac{dT_s}{dx}\right], \tag{9}$$

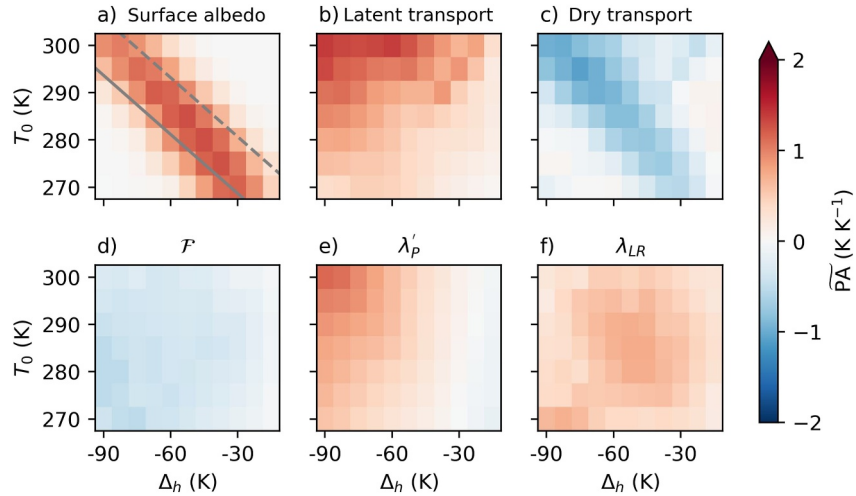

Figure 3. Contributions to $\widetilde{\mathrm{PA}}$ (Equation 4) from the (a) surface albedo feedback, (b) latent energy transport, (c) dry energy transport, (d) radiative forcing, (e) spatially-varying Planck feedback, and (f) lapse rate feedback. Solid (dashed) lines in panel (a) illustrate where the SST at the edge of the polar cap (i.e., 60°) is $T_{\mathrm{edge}} - 6 \approx 256$ K ($T_{\mathrm{edge}} + 6 \approx 268$ K) in the control climate.

where x is the sine of latitude, s is the dry static energy, c_p is the specific heat at constant pressure, and $\mathcal{D}$ is a diffusivity (e.g., North et al., 1981). The divergence of dry static energy transport is thus proportional to the Laplacian of T_s, meaning local perturbations to surface temperature will yield a local compensation through changes in dry transport. Specifically, a local temperature increase (e.g., through the surface albedo feedback) will yield an anomalous divergence of dry static energy, which will act to cool the region.

Similarly diffusive arguments for the divergence of latent energy transport have it proportional to the Laplacian of near-surface specific humidity, q, and thus derives its state-dependence from the Clausius Clapeyron relation. That is, the latent energy transport contribution to polar temperature change increases with global-mean temperature and equator-to-pole temperature contrast. This is because a 1 K increase in surface temperature yields a larger change in q at high temperatures than low temperatures (assuming constant relative humidity), so changes in the meridional gradient of q with warming are larger when the base-state meridional temperature gradient is larger and/or the global-mean temperature is large.

The lapse-rate feedback is state-dependent in two ways. First, the surface albedo feedback drives low-level warming and a positive lapse-rate feedback near the ice edge (Feldl et al., 2020). Second, there is a negative tropical lapse-rate feedback which also enhances $\widetilde{\mathrm{PA}}$ according to Equation 4. The negative tropical lapse-rate feedback can be seen in Figure S3 in Supporting Information S1, which shows Figure 2 but without the tropical average removed.

4.3. Energy Budget Contributions to $\widetilde{\mathrm{PA}}$ Across a Wide Range of Climates

These broad insights hold up if we look across the full range of climate states. Figure 3 shows the contribution to $\widetilde{\mathrm{PA}}$ from each of the energy budget terms, as a function of global-mean surface temperature and equator-to-pole temperature contrast in the control climate state; red colors indicate where the local energy budget component contributes to more high-latitude warming and blue colors indicate where the local energy budget component contributes to more low-latitude warming. The sum of the panels in Figure 3 equals Figure 1d.

The latent component of the energy transport has a large state-dependence, and explains the tendency toward stronger $\widetilde{\mathrm{PA}}$ in warm climates with stronger equator-to-pole temperature contrasts (Figure 3b); similar behavior is found in the simulations with fixed surface albedo (Figure S4 in Supporting Information S1). Superimposed on top of this background tendency, the surface albedo feedbacks also adds a positive contribution to $\widetilde{\mathrm{PA}}$ along the locus of climate states connecting the top-left and bottom-right of Figure 3a. In our GCM, the surface albedo varies strongly with temperature between SSTs of $T_{\mathrm{edge}} - 6$ K and $T_{\mathrm{edge}} + 6$ K (Equation 2), and the region of

positive $\widetilde{\mathrm{PA}}$ in Figure 3a roughly corresponds to climates where the polar cap contains SSTs within this interval (in the control simulation). This region is indicated by the solid and dashed gray lines in Figure 3a. The surface albedo contribution to $\widetilde{\mathrm{PA}}$ is negligible in the upper-right of Figure 3a because those climates are ice-free. It is also negligible in the lower-left of Figure 3a because these climates have an ice-edge that sits far outside of the polar cap, an example of such a climate can be seen in Figure 2d. Changes in dry energy transport offset the surface albedo contribution to $\widetilde{\mathrm{PA}}$ across the whole phase space (Figure 3c), but the cancellation is imperfect and the sum of panels (a) and (c) contributes to an increase in $\widetilde{\mathrm{PA}}$, especially in colder climates with smaller equator-to-pole temperature contrasts.

The contributions to $\widetilde{\mathrm{PA}}$ from radiative forcing (Figure 3d), the spatially-varying Planck feedback (Figure 3e), and the lapse-rate feedback (Figure 3f) exhibit weaker state-dependence than the surface albedo and energy transport terms. The spatially-varying component of the Planck feedback augments the state-dependence from latent energy transport. The radiative forcing has a weak state-dependence that somewhat offsets the spatially-varying Planck feedback (for more discussion, see Text S1 in Supporting Information S1), with the net of these processes tends toward stronger $\widetilde{\mathrm{PA}}$ in warm climates with strong meridional temperature gradients. The contribution of the lapse-rate feedback to $\widetilde{\mathrm{PA}}$ is locally enhanced in those climates with a strong surface albedo contribution. This is easier to see in Figure S5 in Supporting Information S1, which shows the difference in the lapse-rate contribution to $\widetilde{\mathrm{PA}}$ in simulations with and without an ice-albedo feedback. The lapse-rate feedback also contributes to $\widetilde{\mathrm{PA}}$ in very warm, ice-free, climates (the upper right of the phase space) due to the negative tropical lapse-rate feedback.

5. Conclusion

Polar amplification is a ubiquitous aspect of contemporary climate change, but its potential state-dependence across climate states is poorly understood. MEBMs suggest that PA should in fact be state-dependent, due to the dependence of atmospheric energy transport on climatological temperature and temperature gradients (Caballero & Langen, 2005). However, it is not clear if these predictions hold up in more complex climate models. Here, we presented the first systematic examination of the state-dependence of PA in GCM simulations of warming, using an idealized aquaplanet GCM.

Our main result is that PA is state-dependent, and that this state-dependence is largely a superposition of two effects. First, PA is generally larger in climates with stronger global-mean temperatures and larger equator-to-pole temperature contrasts. This behavior is a consequence of moist thermodynamics, which leads to a state-dependence of latent energy transport, and is qualitatively consistent with previous MEBM theory (Chang & Merlis, 2023; Merlis & Henry, 2018). Second, the ice-albedo feedback amplifies PA in climates where the climatological ice-edge sits within the polar cap; the contribution of the ice-albedo feedback to local temperature change can be understood with a simple analytical model (Equation 8).

These two effects explain most of the state-dependence of PA in our simulations, but there is also a small role for temperature feedbacks. The Planck feedback also contributes to stronger PA in warm climates with strong equator-to-pole temperature contrasts, an effect which is offset slightly by the state-dependence of radiative forcing. The lapse-rate feedback contributes positively to PA across all climate states, consistent with previous work (e.g., Hahn et al., 2021), but exhibits no substantial state-dependence in our simulations. A close analysis of the zonal-mean structure of temperature change in this set of simulations would be a valuable step toward understanding the lapse-rate feedback and potential connections to atmospheric energy transport (Cronin & Jansen, 2016; Feldl et al., 2020) across climate states.

What do our results imply for the evolution of PA in a warming world? In response to increased CO_2 we expect an increase in T_0 and a weakening of Δ_h, which moves us toward the upper-right of the phase space. Previous work suggests that, across a wide range of climates, the equator-to-pole temperature contrast, Δ_h, weakens at ≈0.5–1 K per degree of global warming (e.g., Caballero & Langen, 2005; Eisenman & Armour, 2024; Kaspi & Showman, 2015). Hence, our experiments imply that the approximately "Earth-like" case in Figure 1d will see a reduction in PA with warming. Weaker PA in a warmer world has been reported in recent studies using comprehensive GCMs (E.-S. Chung et al., 2025; Kay et al., 2024; Zhou et al., 2023), potentially lending support

to this conclusion. However, any agreement should be taken with a grain of salt given the idealized nature of our simulations.

The idealized GCM simulations presented here have been useful for probing the basic physics of polar amplification and its dependence on the background climate state, but in doing so we have omitted important processes. In particular, our simulations do not include a seasonal cycle or a thermodynamic sea ice model. Both seasonality and ice thermodynamics are known to shape PA through affecting the growth and thickness of sea ice (e.g., Feldl & Merlis, 2021), and by affecting the lapse-rate feedback (Hahn et al., 2022). Additionally, our simulations use a clear-sky, gray radiation scheme, which means that radiative feedbacks from clouds and moisture are not represented, even though these are also known to influence the degree of PA in contemporary climate simulations (e.g., Hahn et al., 2021; Kay et al., 2024). Future work could build upon the simulations conducted here by including more realistic representations of radiative transfer (e.g., Manners et al., 2017; Williams, 2025a), and sea ice (e.g., Wagner & Eisenman, 2015), and by including seasonality, realistic geography, and a dynamic ocean. Such a research program would be a fruitful avenue toward understanding the full state-dependence of polar amplification.

Conflict of Interest

The authors declare no conflicts of interest relevant to this study.

Data Availability Statement

A Zenodo repository with the Isca model source code, and analysis code to reproduce the figures is available at Williams (2025b).

Acknowledgments
A.I.L. Williams acknowledges funding from the CIMES Postdoctoral Fellowship under award NA18OAR4320123 from the National Oceanic and Atmospheric Administration, U.S. Department of Commerce. This research was supported in part by Grant NSF PHY-2309135 to the Kavli Institute for Theoretical Physics (KITP). The simulations presented in this paper were performed using High Performance Computing resources provided by the Cooperative Institute for Modeling the Earth System. We are grateful to Neil Lewis, Stephen Thomson, and Tra Dinh for technical assistance with configuring and running Isca. We thank Lily Hahn, Rodrigo Caballero, and Nicole Feldl for scientific feedback, and Sampson Schamerhorn for encouragement. Helpful comments from Kris Karnauskas and two anonymous reviewers greatly improved the clarity and content of this manuscript.

References

Bonan, D. B., Armour, K. C., Roe, G. H., Siler, N., & Feldl, N. (2018). Sources of uncertainty in the meridional pattern of climate change. *Geophysical Research Letters*, *45*(17), 9131–9140. https://doi.org/10.1029/2018gl079429

Caballero, R., & Langen, P. L. (2005). The dynamic range of poleward energy transport in an atmospheric general circulation model. *Geophysical Research Letters*, *32*(2), L02705. https://doi.org/10.1029/2004GL021581

Chang, C.-Y., & Merlis, T. M. (2023). The role of diffusivity changes on the pattern of warming in energy balance models. *Journal of Climate*, *36*(22), 7993–8006. https://doi.org/10.1175/jcli-d-23-0121.1

Chung, E.-S., Kim, S.-J., Ha, K.-J., Stuecker, M. F., Lee, S.-S., Kim, J.-H., et al. (2025). The role of sea ice in present and future arctic amplification. *Communications Earth & Environment*, *6*(1), 910. https://doi.org/10.1038/s43247-025-02834-9

Chung, P.-C., & Feldl, N. (2024). Sea ice loss, water vapor increases, and their interactions with atmospheric energy transport in driving seasonal polar amplification. *Journal of Climate*, *37*(8), 2713–2725. https://doi.org/10.1175/jcli-d-23-0219.1

Cronin, T. W., & Jansen, M. F. (2016). Analytic radiative-advective equilibrium as a model for high-latitude climate. *Geophysical Research Letters*, *43*(1), 449–457. https://doi.org/10.1002/2015gl067172

Crook, J. A., Forster, P. M., & Stuber, N. (2011). Spatial patterns of modeled climate feedback and contributions to temperature response and polar amplification. *Journal of Climate*, *24*(14), 3575–3592. https://doi.org/10.1175/2011jcli3863.1

Deser, C., Tomas, R., Alexander, M., & Lawrence, D. (2010). The seasonal atmospheric response to projected Arctic sea ice loss in the late twenty-first century. *Journal of Climate*, *23*(2), 333–351. https://doi.org/10.1175/2009jcli3053.1

Eisenman, I., & Armour, K. C. (2024). The radiative feedback continuum from snowball earth to an ice-free hothouse. *Nature Communications*, *15*(1), 6582. https://doi.org/10.1038/s41467-024-50406-w

Eisenman, I., & Wettlaufer, J. (2009). Nonlinear threshold behavior during the loss of arctic sea ice. *Proceedings of the National Academy of Sciences*, *106*(1), 28–32. https://doi.org/10.1073/pnas.0806887106

England, M. R., Eisenman, I., & Wagner, T. J. (2022). Spurious climate impacts in coupled sea ice loss simulations. *Journal of Climate*, *35*(22), 7401–7411. https://doi.org/10.1175/jcli-d-21-0647.1

Feldl, N., & Merlis, T. M. (2021). Polar amplification in idealized climates: The role of ice, moisture, and seasons. *Geophysical Research Letters*, *48*(17), e2021GL094130. https://doi.org/10.1029/2021gl094130

Feldl, N., Po-Chedley, S., Singh, H. K. A., Hay, S., & Kushner, P. J. (2020). Sea ice and atmospheric circulation shape the high-latitude lapse rate feedback. *npj Climate and Atmospheric Science*, *3*, 1–9. https://doi.org/10.1038/s41612-020-00146-7

Feldl, N., & Roe, G. H. (2013). The nonlinear and nonlocal nature of climate feedbacks. *Journal of Climate*, *26*(21), 8289–8304. https://doi.org/10.1175/jcli-d-12-00631.1

Flannery, B. P. (1984). Energy balance models incorporating transport of thermal and latent energy. *Journal of the Atmospheric Sciences*, *41*(3), 414–421. https://doi.org/10.1175/1520-0469(1984)041<0414:ebmito>2.0.co;2

Frierson, D. M. W. (2007). The dynamics of idealized convection schemes and their effect on the zonally averaged tropical circulation. *Journal of the Atmospheric Sciences*, *64*(6), 1959–1976. https://doi.org/10.1175/jas3935.1

Frierson, D. M. W., Held, I. M., & Zurita-Gotor, P. (2006). A gray-radiation aquaplanet moist GCM. Part I: Static stability and eddy scale. *Journal of the Atmospheric Sciences*, *63*(10), 2548–2566. https://doi.org/10.1175/jas3753.1

Guendelman, I., & Kaspi, Y. (2020). Atmospheric dynamics on terrestrial planets with eccentric orbits. *The Astrophysical Journal*, *901*(1), 46. https://doi.org/10.3847/1538-4357/abaef8

Hahn, L. C., Armour, K. C., Battisti, D. S., Donohoe, A., & Fajber, R. (2023). Seasonal changes in atmospheric heat transport to the Arctic under increased CO_2. *Geophysical Research Letters*, *50*(20), e2023GL105156. https://doi.org/10.1029/2023gl105156

Hahn, L. C., Armour, K. C., Battisti, D. S., Eisenman, I., & Bitz, C. M. (2022). Seasonality in arctic warming driven by sea ice effective heat capacity. *Journal of Climate*, *35*(5), 1629–1642. https://doi.org/10.1175/jcli-d-21-0626.1

Hahn, L. C., Armour, K. C., Zelinka, M. D., Bitz, C. M., & Donohoe, A. (2021). Contributions to polar amplification in CMIP5 and CMIP6 models. *Frontiers in Earth Science*, *9*, 710036. https://doi.org/10.3389/feart.2021.710036

Held, I. M., Delworth, T. L., Lu, J., Findell, K. L., & Knutson, T. R. (2005). Simulation of Sahel drought in the 20th and 21st centuries. *Proceedings of the National Academy of Sciences*, *102*(50), 17891–17896. https://doi.org/10.1073/pnas.0509057102

Henry, M., & Merlis, T. M. (2019). The role of the nonlinearity of the Stefan-Boltzmann law on the structure of radiatively forced temperature change. *Journal of Climate*, *32*(2), 335–348. https://doi.org/10.1175/jcli-d-17-0603.1

Henry, M., & Vallis, G. K. (2022). Variations on a pathway to an early Eocene climate. *Paleoceanography and Paleoclimatology*, *37*(8), e2021PA004375. https://doi.org/10.1029/2021pa004375

Holland, M. M., & Bitz, C. M. (2003). Polar amplification of climate change in coupled models. *Climate Dynamics*, *21*(3), 221–232. https://doi.org/10.1007/s00382-003-0332-6

Huber, M., & Caballero, R. (2011). The early Eocene equable climate problem revisited. *Climate of the Past*, *7*(2), 603–633. https://doi.org/10.5194/cp-7-603-2011

Hwang, Y.-T., Frierson, D. M. W., & Kay, J. E. (2011). Coupling between Arctic feedbacks and changes in poleward energy transport. *Geophysical Research Letters*, *38*(17), L17704. https://doi.org/10.1029/2011gl048546

Jeevanjee, N., Hassanzadeh, P., Hill, S., & Sheshadri, A. (2017). A perspective on climate model hierarchies. *Journal of Advances in Modeling Earth Systems*, *9*(4), 1760–1771. https://doi.org/10.1002/2017ms001038

Judd, E. J., Tierney, J. E., Lunt, D. J., Montañez, I. P., Huber, B. T., Wing, S. L., & Valdes, P. J. (2024). A 485-million-year history of earth's surface temperature. *Science*, *385*(6715), eadk3705. https://doi.org/10.1126/science.adk3705

Kaspi, Y., & Showman, A. P. (2015). Atmospheric dynamics of terrestrial exoplanets over a wide range of orbital and atmospheric parameters. *The Astrophysical Journal*, *804*(1), 60. https://doi.org/10.1088/0004-637x/804/1/60

Kay, J. E., Liang, Y.-C., Zhou, S.-N., & Maher, N. (2024). Sea ice feedbacks cause more greenhouse cooling than greenhouse warming at high northern latitudes on multi-century timescales. *Environmental Research: Climate*, *3*(4), 041003. https://doi.org/10.1088/2752-5295/ad8026

Kluft, L., Dacie, S., Buehler, S. A., Schmidt, H., & Stevens, B. (2019). Re-examining the first climate models: Climate sensitivity of a modern radiative–convective equilibrium model. *Journal of Climate*, *32*(23), 8111–8125. https://doi.org/10.1175/jcli-d-18-0774.1

Langen, P. L., Graversen, R. G., & Mauritsen, T. (2012). Separation of contributions from radiative feedbacks to polar amplification on an aquaplanet. *Journal of Climate*, *25*(8), 3010–3024. https://doi.org/10.1175/jcli-d-11-00246.1

Lu, J., & Cai, M. (2009). A new framework for isolating individual feedback processes in coupled general circulation climate models. Part I: Formulation. *Climate Dynamics*, *32*(6), 873–885. https://doi.org/10.1007/s00382-008-0425-3

Lu, J., Zhou, W., Kong, H., Leung, L. R., Harrop, B., & Song, F. (2022). On the diffusivity of moist static energy and implications for the polar amplification response to climate warming. *Journal of Climate*, *35*(21), 3521–3540. https://doi.org/10.1175/jcli-d-21-0721.1

Maher, P., Gerber, E. P., Medeiros, B., Merlis, T. M., Sherwood, S., Sheshadri, A., et al. (2019). Model hierarchies for understanding atmospheric circulation. *Reviews of Geophysics*, *57*(2), 250–280. https://doi.org/10.1029/2018rg000607

Manabe, S., & Stouffer, R. J. (1980). Sensitivity of a global climate model to an increase of co2 concentration in the atmosphere. *Journal of Geophysical Research*, *85*(C10), 5529–5554. https://doi.org/10.1029/jc085ic10p05529

Manners, J., Edwards, J. M., Hill, P., & Thelen, J.-C. (2017). Socrates technical guide: Suite of community radiative transfer codes based on edwards and slingo (Tech. Rep.). *Technical Report, Met Office, Exeter, UK*.

Masson-Delmotte, V., Kageyama, M., Braconnot, P., Charbit, S., Krinner, G., Ritz, C., et al. (2006). Past and future polar amplification of climate change: Climate model intercomparisons and ice-core constraints. *Climate Dynamics*, *26*(5), 513–529. https://doi.org/10.1007/s00382-005-0081-9

Merlis, T. M., Feldl, N., & Caballero, R. (2022). Changes in poleward atmospheric energy transport over a wide range of climates: Energetic and diffusive perspectives and a priori theories. *Journal of Climate*, *35*(20), 2933–2948. https://doi.org/10.1175/jcli-d-21-0682.1

Merlis, T. M., & Henry, M. (2018). Simple estimates of polar amplification in moist diffusive energy balance models. *Journal of Climate*, *31*(15), 5811–5824. https://doi.org/10.1175/jcli-d-17-0578.1

Mlawer, E. J., Taubman, S. J., Brown, P. D., Iacono, M. J., & Clough, S. A. (1997). Radiative transfer for inhomogeneous atmospheres: RRTM, a validated correlated-k model for the longwave. *Journal of Geophysical Research*, *102*(D14), 16663–16682. https://doi.org/10.1029/97jd00237

North, G. R., Cahalan, R. F., & Coakley, J. A. (1981). Energy balance climate models. *Reviews of Geophysics*, *19*(1), 91–121. https://doi.org/10.1029/rg019i001p00091

O'Gorman, P. A., & Schneider, T. (2008a). Energy of midlatitude transient eddies in idealized simulations of changed climates. *Journal of Climate*, *21*(22), 5797–5806. https://doi.org/10.1175/2008jcli2099.1

O'Gorman, P. A., & Schneider, T. (2008b). The hydrological cycle over a wide range of climates simulated with an idealized GCM. *Journal of Climate*, *21*(15), 3815–3832. https://doi.org/10.1175/2007jcli2065.1

Pierrehumbert, R., Abbot, D. S., Voigt, A., & Koll, D. (2011). Climate of the neoproterozoic. *Annual Review of Earth and Planetary Sciences*, *39*(1), 417–460. https://doi.org/10.1146/annurev-earth-040809-152447

Roe, G. H., Feldl, N., Armour, K. C., Hwang, Y.-T., & Frierson, D. M. W. (2015). The remote impacts of climate feedbacks on regional climate predictability. *Nature Geoscience*, *8*(2), 135–139. https://doi.org/10.1038/ngeo2346

Rose, B. E. J., Armour, K. C., Battisti, D. S., Feldl, N., & Koll, D. D. B. (2014). The dependence of transient climate sensitivity and radiative feedbacks on the spatial pattern of ocean heat uptake. *Geophysical Research Letters*, *41*(3), 1071–1078. https://doi.org/10.1002/2013gl058955

Taylor, P. C., Boeke, R. C., Boisvert, L. N., Feldl, N., Henry, M., Huang, Y., et al. (2022). Process drivers, inter-model spread, and the path forward: A review of amplified Arctic warming. *Frontiers in Earth Science*, *9*, 758361. https://doi.org/10.3389/feart.2021.758361

Vallis, G. K., Colyer, G., Geen, R., Gerber, E., Jucker, M., Maher, P., et al. (2018). Isca, v1.0: A framework for the global modelling of the atmospheres of earth and other planets at varying levels of complexity. *Geoscientific Model Development*, *11*(3), 843–859. https://doi.org/10.5194/gmd-11-843-2018

Wagner, T. J. W., & Eisenman, I. (2015). How climate model complexity influences sea ice stability. *Journal of Climate*, *28*(10), 3998–4014. https://doi.org/10.1175/jcli-d-14-00654.1

Williams, A. I. (2025a). Bridging clarity and accuracy: A simple spectral longwave radiation scheme for idealized climate modeling. *arXiv preprint arXiv:2508.09353*.

Williams, A. I. (2025b). Supporting data for "state-dependence of polar amplification in an idealized gcm" [dataset]. *Zenodo*. https://doi.org/10.5281/zenodo.17527346

Winton, M. (2006). Amplified Arctic climate change: What does surface albedo feedback have to do with it? *Geophysical Research Letters*, *33*(3), L03701. https://doi.org/10.1029/2005gl025244

Zhou, S.-N., Liang, Y.-C., Mitevski, I., & Polvani, L. M. (2023). Stronger arctic amplification produced by decreasing, not increasing, co2 concentrations. *Environmental Research: Climate*, *2*(4), 045001. https://doi.org/10.1088/2752-5295/aceea2